

# **Broadband superluminescent diode–based ultrahigh resolution optical coherence tomography for ophthalmic imaging**

Dexi Zhu  
Meixiao Shen  
Hong Jiang  
Ming Li  
Michael R. Wang  
Yuhong Wang  
Lili Ge  
Jia Qu  
Jianhua Wang

# Broadband superluminescent diode–based ultrahigh resolution optical coherence tomography for ophthalmic imaging

Dexi Zhu,<sup>a,b</sup> Meixiao Shen,<sup>b</sup> Hong Jiang,<sup>b</sup> Ming Li,<sup>a,b</sup> Michael R. Wang,<sup>c</sup> Yuhong Wang,<sup>a,b</sup> Lili Ge,<sup>a,b</sup> Jia Qu,<sup>a</sup> and Jianhua Wang<sup>b</sup>

<sup>a</sup> Wenzhou Medical College, School of Ophthalmology and Optometry, Wenzhou, Zhejiang 325000, China

<sup>b</sup> University of Miami, Bascom Palmer Eye Institute, Miami, Florida 33136

<sup>c</sup> University of Miami, Department of Electrical and Computer Engineering, Miami, Florida 33136

**Abstract.** Spectral domain optical coherence tomography (SD-OCT) with ultrahigh resolution can be used to measure precise structures in the context of ophthalmic imaging. We designed an ultrahigh resolution SD-OCT system based on broadband superluminescent diode (SLD) as the light source. An axial resolution of 2.2  $\mu\text{m}$  in tissue, a scan depth of 1.48 mm, and a high sensitivity of 93 dB were achieved by the spectrometer designed. The ultrahigh-resolution SD-OCT system was employed to image the human cornea and retina with a cross-section image of 2048  $\times$  2048 pixels. Our research demonstrated that ultrahigh-resolution SD-OCT can be achieved using broadband SLD in a simple way. © 2011 Society of Photo-Optical Instrumentation Engineers (SPIE). [DOI: 10.1117/1.3660314]

Keywords: optical coherence tomography; ophthalmic imaging.

Paper 11343R received Jul. 5, 2011; revised manuscript received Sep. 30, 2011; accepted for publication Oct. 24, 2011; published online Nov. 28, 2011.

## 1 Introduction

Optical coherence tomography (OCT) is a cross-sectional imaging technology that has been used to image biological tissue and materials with high-resolution in a noninvasive manner.<sup>1,2</sup> OCT has been especially useful for ophthalmic imaging because the eye is composed of a series of transparent structures from the cornea to the retina, creating a natural optical detecting path. Recently, spectral domain OCT (SD-OCT) has been demonstrated to have ultrahigh resolution and greater speed compared with time domain OCT and has been widely applied to ophthalmic imaging.<sup>3–13</sup> In SD-OCT, the structural information is obtained by measuring the backscattered or backreflected light by means of spectral analysis of the interference pattern.

The performances of OCT, such as resolution, system sensitivity, light penetration, and scanning speed, have a significant impact on medical imaging. Among all of these, axial resolution is a key factor contributing to imaging performance, especially when OCT is applied for ophthalmic imaging because there are many lamellar structures with micrometer-range thickness in both the anterior and posterior segments of the eyes. Subtle changes involving less than a couple of micrometers occur during early onset or yearly follow-up of some ophthalmic diseases. For example, thinning of the retinal nerve fiber layer was found to occur at a rate of only 2  $\mu\text{m}$  per year in multiple sclerosis (MS) patients without optic neuritis.<sup>14–16</sup> The anterior segment of the eye demands high-resolution imaging due to the significance of layers, such as the natural state of the tear film (a few micrometers in thickness) or post-contact lens (CL) wear measurements of the tear film, which may be less than 3  $\mu\text{m}$ .

Commercially available OCT devices have an axial resolution of about 3 to 5  $\mu\text{m}$ , which may not be enough to detect subtle changes in layers.

Based on the previous works on ophthalmic imaging by OCT,<sup>17–21</sup> an ultrahigh resolution SD-OCT using an extremely broadband superluminescent diode (SLD) at the central wavelength of 870 nm as the light source is demonstrated in this paper. An axial resolution of 3.1  $\mu\text{m}$  in air (2.2  $\mu\text{m}$  in tissue) was achieved by this OCT system. It is the highest resolution of SLD-based OCT as we know. Other performances of this SD-OCT setup, such as sensitivity and dynamic range, were also measured. We attempt to track the post-lens tear exchange and to image more retinal layers using this ultrahigh resolution OCT. It may further enlarge the application of OCT on ophthalmic research for imaging the layers that require high axial resolution.

## 2 Experimental Setup and Method

### 2.1 Instrument

The OCT system (Fig. 1) is composed of four parts: a light source, reference arm, sample arm, and spectrometer. The light source is a broadband three-module superluminescent diode (T870-HP, Superlum, Ireland), which has a 188-nm bandwidth according to the manufacturer, and is centered at a wavelength of 870 nm. The power of incident light on the human eye is equal to 750  $\mu\text{W}$ , as dictated by the safety standards by the American National Standards Institute. The light is split into the reference arm and sample arm by a 50:50 fiber coupler. The sample arm is interfaced to a slit-lamp microscope for convenient adjustment during imaging alignment. When retinal imaging is performed, an additional ocular lens (Volk 60D) is inserted in the sample arm. An internal fixation target displayed on a liquid crystal

Address all correspondence to: Jianhua Wang, University of Miami Miller School of Medicine, Bascom Palmer Eye Institute, Department of Ophthalmology, 1638 NW, 10th Avenue, Miami, Florida 33136; Tel: 305-482-5011; Fax: 305-482-5011; E-mail: jwang3@med.miami.edu.

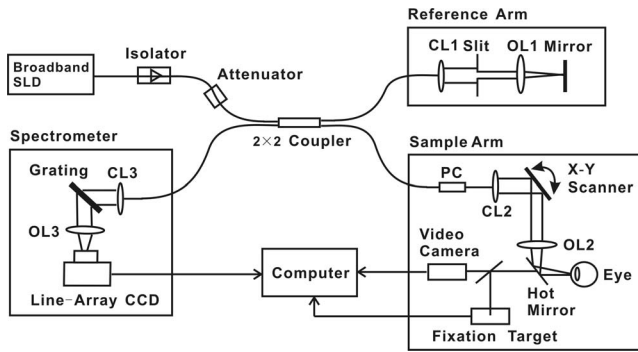


**Fig. 1** Schematic diagram of the ultrahigh resolution spectral-domain OCT system. The retina is imaged by using an additional ocular lens (Volk 60D) in front of the eye. CL1–CL3: collimating lenses; OL1–OL3: objective lenses; PC: polarization controller.

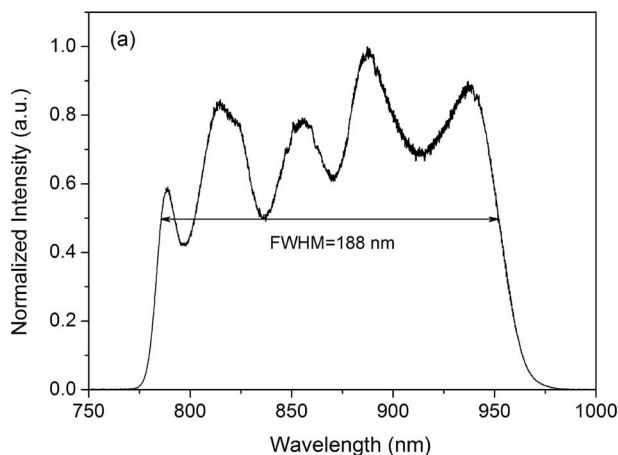
display monitor was employed to control the position of the subject's eye. Dispersion matching between the sample arm and reference arm is performed using a set of optical materials (BK7 glass), which are inserted in the reference light path for dispersion compensation. Dispersion matching is especially critical for imaging the posterior segment of the eye.

The spectrum of the interference signal was detected by a spectrometer consisting of a collimating lens, a 1200 lines/mm volume holography transmission grating, an achromatic imaging lens with a focal length of 75 mm (Rolyn Optics, Covina, California), and a line array CCD camera (Aviiva SM2). The CCD camera has 2048 pixels with a 14- $\mu\text{m}$  pixel interval and a 24-kHz data transfer rate. The acquired interference spectrum data was transferred to a computer system using a National Instrument image acquisition card (PCI 1428). Data processing was performed using custom-built software.

## 2.2 Resolution

As a sort of interferometer, the axial resolution of OCT is determined by the coherence length of the light source, which is the Fourier transfer of the power spectrum of the light source. The axial resolution in air is given as<sup>22</sup>

$$\Delta z = \frac{2 \ln 2 \lambda_0^2}{\pi \Delta \lambda}, \quad (1)$$



where  $\lambda_0$  is the central wavelength and  $\Delta \lambda$  is the full width at half-maximum (FWHM) bandwidth.

A low central wavelength and a broadband light source are required to improve the axial resolution. In our experiment, a broadband SLD was employed as the low-coherence light source. As shown in Fig. 2(a), the FWHM bandwidth of the SLD was 188 nm. However, the available bandwidth was narrower than this value because the bandwidth of the fiber optic components, such as the fiber coupler and attenuator, limited the full use of the broad bandwidth of the light source. Furthermore, the profile of the light spectrum was not perfectly Gaussian, so the effective axial resolution of the OCT system would not be calculated directly from Eq. (1). In order to obtain the real axial resolution, the point spread function (PSF) was measured by imaging a mirror at different positions. The FWHM of the PSF, which indicates the resolution of the OCT system, increases as the mirror position is moved farther away from the optical zero delay plane. The PSF at a path length difference of 0.2 mm was 3.1  $\mu\text{m}$  in air. The corresponding axial resolution in tissue was about 2.2  $\mu\text{m}$  as shown in Fig. 2(b), assuming the refractive index of the tissue (cornea and retina) is 1.38.

## 2.3 Scan Depth

In SD-OCT, the spectral range detected by the line-array CCD limits the axial resolution. The spectral range should be large enough to ensure the entire bandwidth of the light source can be detected in the spectrometer. Otherwise, the axial resolution cannot be determined by Eq. (1). In order to achieve optimal resolution, the spectrometer must be designed appropriately, and the spectral resolution must be calculated. The spectral resolution of the OCT spectrometer is determined by the resolution of both the CCD and diffraction grating. The resolution of CCD indicates the wavelength range occupied by one CCD pixel, which is determined by:<sup>23</sup>

$$\delta \lambda_c = \frac{dp \cos \theta}{mf}, \quad (2)$$

where  $p$  is the pixel interval of the CCD array ( $p = 14 \mu\text{m}$ ),  $d$  is the grating period ( $d = 1/1200 \text{ mm}$ ),  $m$  is the diffraction order ( $m = 1$ ),  $\theta$  is the diffraction angle ( $\theta = 32^\circ$ ), and  $f$  is the focal

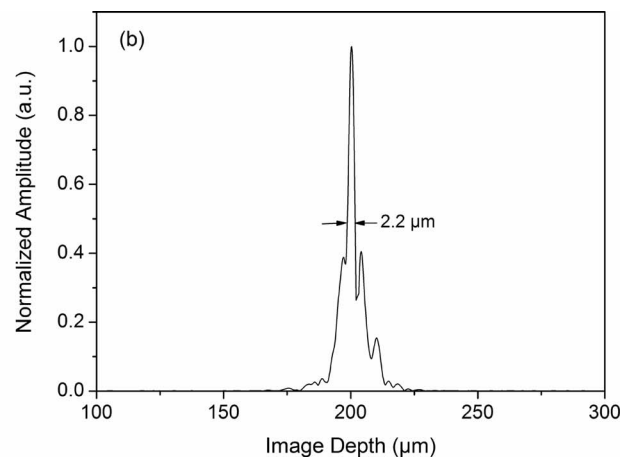


**Fig. 2** (a) Spectrum of the SLD used in the OCT system. The FWHM bandwidth was 188 nm. (b) Point-spread function obtained from a mirror at a path length difference of 0.2 mm. The measured resolution at this position is 3.1  $\mu\text{m}$  in air, corresponding to 2.2  $\mu\text{m}$  in tissue (refractive index: 1.38).

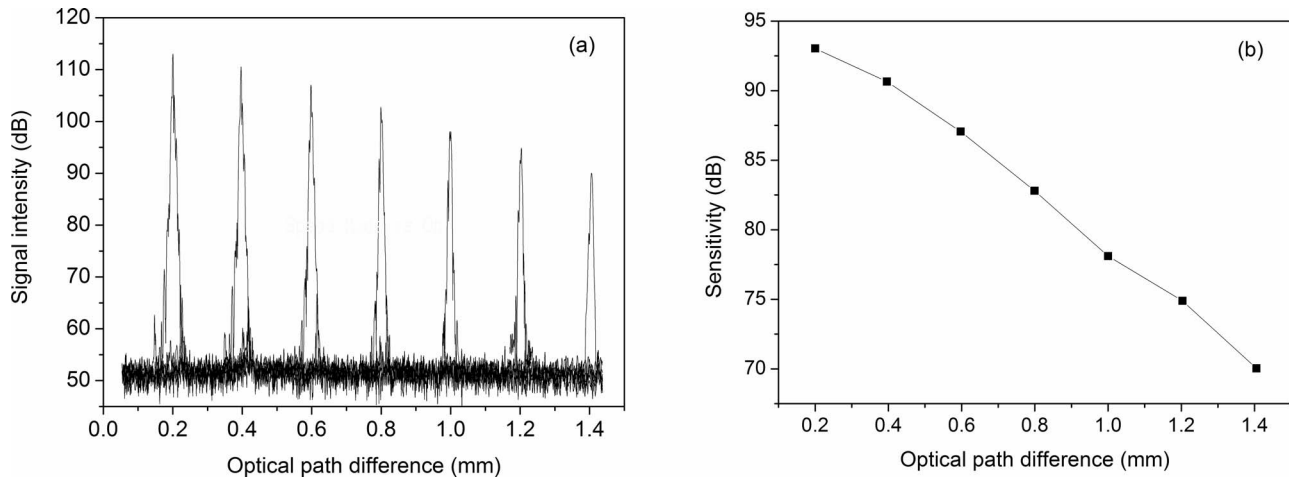


**Fig. 3** Axial response signal on a logarithmic scale (a) and sensitivity (b) at different image depth from the zero-delay plane.

length of the imaging lens, which focuses the diffraction light on the CCD ( $f = 75$  mm). Using these parameters in Eq. (2), the spectral resolution of CCD is calculated to be 0.135 nm. The spectral resolution of the diffraction grating is expressed as:<sup>24</sup>

$$\delta\lambda_g = \frac{\lambda_0 d \cos \theta_0}{mD}, \quad (3)$$

where  $\lambda_0$  is the central wavelength,  $D$  is the diameter of the beam that illuminated the grating, and  $\theta_0$  is the blaze angle, which is determined by the Bragg condition for a diffraction grating, which is expressed as  $\sin \theta_0 = \lambda_0 / (2d)$ . Based on Eq. (3), the spectral resolution of the grating is 0.062 nm. The spectral resolution of the spectrometer ( $\delta\lambda$ ) is the larger of the two values, i.e., the spectral resolution of the CCD.

Based on the spectral resolution of the spectrometer, the axial scan depth can be determined by

$$\Delta l_z = \frac{\lambda_0^2}{4n\Delta\lambda}, \quad (4)$$

where  $n$  is the refractive index of the sample. The scan depth is about 1.48 mm in air, which is consistent with the measured value. Therefore, if the OCT image is acquired using an image size of  $2048 \times 2048$  pixels/frame, then the axial pixel spacing in the image is about  $0.68 \mu\text{m}$ , which is less than the measured axial resolution above. Therefore, this spectrometer design was able to support ultrahigh resolution.

#### 2.4 Sensitivity

Detection sensitivity is a significant aspect of SD-OCT performance. Because most biological tissues are not highly scattering, the intensity of light backscattered or backreflected from the imaged tissues is extremely low. The sensitivity determines the image contrast and the maximum possible imaging depth. We measured the sensitivity of the OCT system by detecting the interference signal of a mirror at different depth positions. A neutral density filter with optical density (OD) of 1.5 is placed in the sample arm to reduce the signal intensity. After processing with zero padding and Fourier transformation,<sup>25,26</sup> the axial response was represented in a logarithmic scale as a function of optical path difference [Fig. 3(a)]. It shows that the signal peak decreased as the image depth increased, indicating the signal-to-noise ratio (SNR) of the OCT system decreased as the position

moved farther away from the zero delay plane. The dynamic range of this system, which was about 65 dB at the depth of 0.2 mm, was also found from Fig. 3(a).

The sensitivity was calculated from SNR as

$$\text{sensitivity} = 10 \cdot \log \left( \frac{S}{\sigma} \right) + 20 \cdot OD, \quad (5)$$

where  $S$  is the signal peak in Fig. 3(a),  $\sigma$  is the noise, and OD is 1.5. As shown in Fig. 3(b), the sensitivity decreases from 93 to 70 dB as the optical path difference increases from 0.2 to 1.4 mm. This sensitivity drop is an essential defect in SD-OCT. However, in our OCT system, the sensitivity is high enough to detect weak signals in different image positions. It also indicates that the scan depth range of 1.4 mm is acceptable because the sensitivity may be too low in deeper positions, and the image contrast will not be high enough to distinguish tiny differences in the sample.

### 3 Imaging of the Human Eye

#### 3.1 Imaging the Anterior Segment of the Human Eye

We use this SD-OCT to image the anterior and posterior segments of human eyes. The exposure time of a single line of the CCD was set to  $36 \mu\text{s}$ , corresponding to a scan rate of 24,000 A-scans/s. Therefore, the imaging speed was about 12 frames/s when acquiring an image of  $2048 \times 2048$  pixels.

Figure 4 shows an ultrahigh resolution OCT image of the anterior segment of the human eye. Custom software was used to correct the image caused by refraction at the air-cornea interface. The zero delay plane was set at the top of the image; hence, the anterior surface of the cornea was the region of

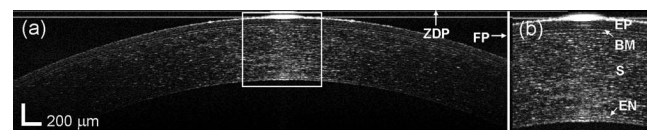


**Fig. 4** OCT image of the anterior segment (a) and the magnified images at the apex (b). EP: epithelium; BM: Bowman's membrane; S: stroma; EN: endothelium.

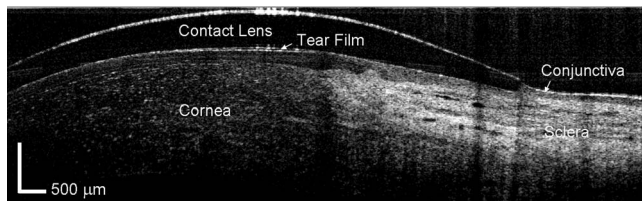


**Fig. 5** OCT image of the limbus region underneath a contact lens. The lens edge and post-lens tear film were visualized clearly.

highest sensitivity. In the peripheral region of the cornea, the resolution and contrast were reduced because of the curved shape of the cornea. Certain components of the cornea, such as the epithelium, Bowman’s membrane, stroma, and endothelium, were clearly presented in a magnified image of the central cornea, as shown in Fig. 4(b).

The edge of a contact lens on the eye was imaged by ultrahigh resolution OCT, as shown in Fig. 5. The conjunctiva and the junction between the cornea and the sclera were visualized. A gap between the corneal epithelium and contact lens was also clear and filled with post-lens tears. This tear film was about 10 μm thick, as measured in the image.

The post-CL tear film may also play a role in CL fitting and ocular comfort. However, the relationship between ocular comfort and tear dynamics remains unclear, mainly due to the lack of an efficient tool for tracking the tear volume and tear exchange underneath the CL. The post-CL tear film is about

2-μm thick in the center and usually more than 10-μm thick in the post-CL gaps.<sup>17</sup> The thick gaps provide an opportunity for tracking tear exchange using OCT-scattering media to image the post-CL tear film gap (post-CL gap), as shown in Fig. 6. After the OCT-scattering media was instilled on the surface of CL, the scattering media was infiltrated from the surface into the post-CL gap, as shown in Figs. 6(b) and 6(c). One minute later, the tear film gap was imaged again at the same position. Figure 6(d) shows that the scattering media has been diluted because of the existence of tear exchange between anterior and post lens tear film. This experiment demonstrates that ultrahigh resolution OCT can be applied in the research of CL fitting and ocular comfort.

### 3.2 Imaging the Posterior Segment of the Human Eye

For retinal imaging, an ocular lens was added in front of the eye in the sample arm. Figure 7 shows an ultrahigh resolution OCT image in gray scale of the human retina in the region of the macula. Three structures (vitreous, retina, and choroid) are presented in this image. In the retina, a total of nine structural layers can be identified by the brightness of the pixels, as shown in Fig. 7(a). A narrow white line at the bottom of the outer nuclear layer is the external limiting membrane, which is usually not recognized by commercially available OCT systems. The cloudy structure at the bottom of the image is the choroid, where cross-sections of vascular structures are visible. Based on this

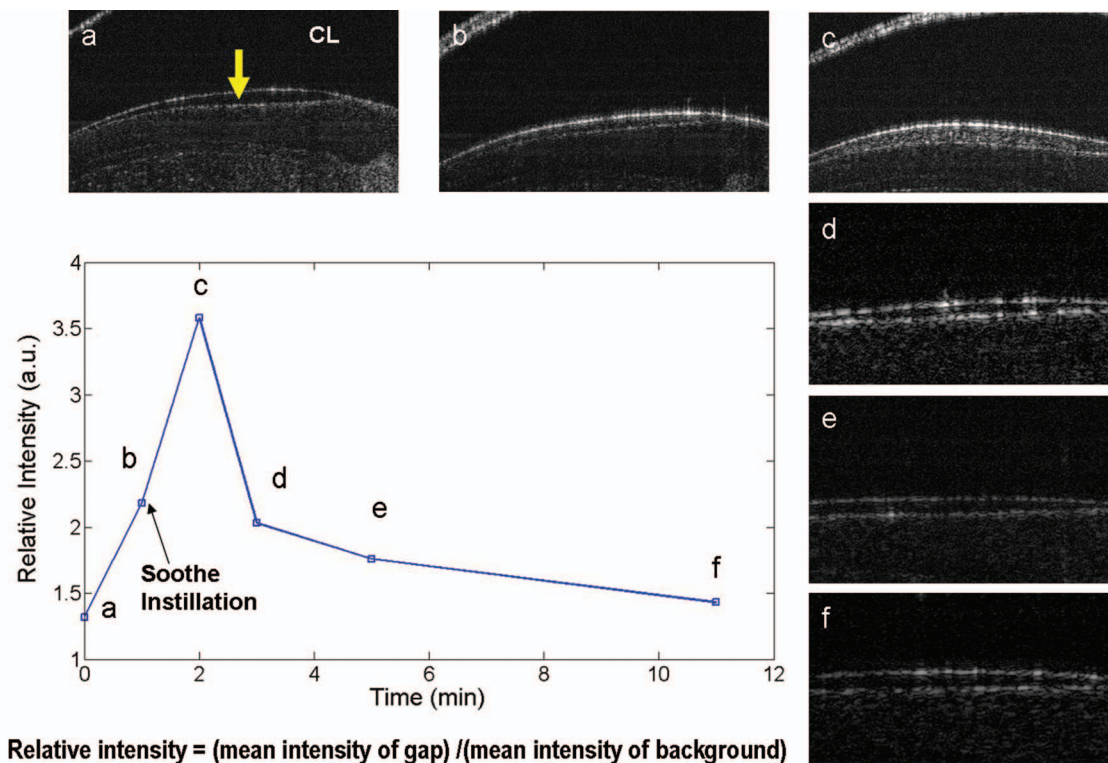


**Fig. 6** Tracking tear exchange underneath the lens. The post-CL gap (yellow arrow) was imaged using our newly developed ultrahigh resolution OCT before and after the instillation of OCT-scattering media (Soothe XP, Bausch & Lomb, Rochester, New York). The light scattering from the 10 × 10 pixels within the gap was quantified and normalized by the background noise. The intensity of the scattering was used to quantify the mixing/exchanging of the tears with the scattering media. The increase of scattering was evident in OCT images after instillation of the media. The inserted graph showed calculated intensity of the scattering in the post-lens tear film, which demonstrated possible tear exchange.

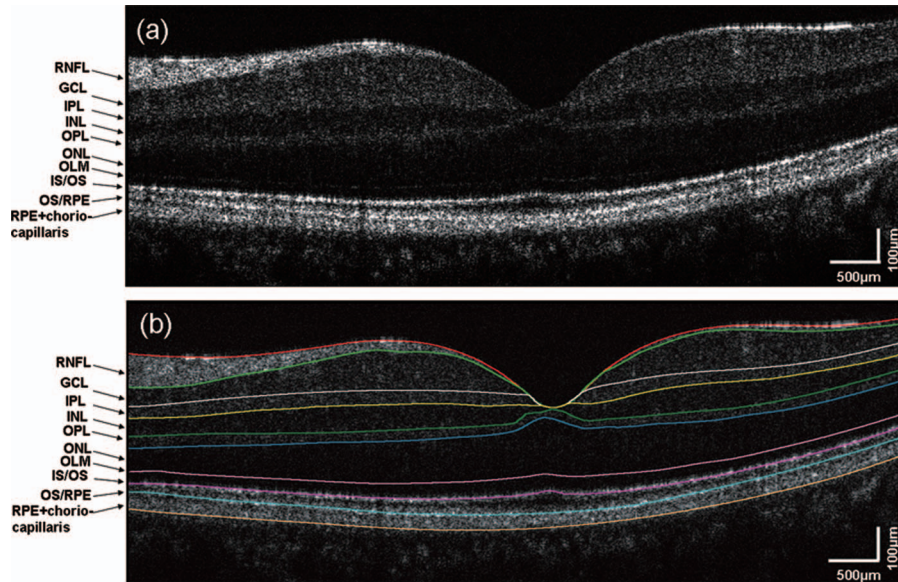


**Fig. 7** Human macular image acquired by SD-OCT. Retinal sublayers are visualized clearly (a) and can be segmented using the semiautomatic method (b). These sublayers are the RNFL, ganglion cell layer (GCL), inner plexiform layer (IPL), inner nuclear layer (INL), outer plexiform layer (OPL), outer nuclear layer (ONL), outer limiting membrane (OLM), inner segment layer/outer segment layer junction (IS/OS), outer segment layer/retinal pigment epithelium junction (OS/RPE), and RPE + choriocapillaris.

picture, we can segment these layers in order to measure the thicknesses of each [Fig. 7(b)]. In Fig. 8, an optic nerve head was imaged. In the *en face* view of optic nerve head, the artery, vein, cup, and optic disk are clearly visualized. In the horizontal cross-sectional OCT image, the cup and disk are identified, and the cup/disk ratio is calculated to be 0.73.

#### 4 Discussion

Axial resolution is theoretically determined by the central wavelength and bandwidth of the OCT system's light source: the resolution increases for wider bandwidth and lower central wavelength. The quality of the light source also affects the ability of the light to penetrate strongly scattering tissue. Therefore,

the selection of a particular light source for OCT is significant for high resolution and deep penetration. Ti:sapphire lasers have been used for ultrahigh resolution OCT.<sup>22,27,28</sup> Based on the extremely broad bandwidth of spectra in the 800-nm wavelength region, OCT using Ti:sapphire lasers as a light source achieve the highest resolution of about 1  $\mu\text{m}$ .<sup>24,29-32</sup> However, the application of a Ti:sapphire laser in commercial OCT is limited because of their complexity and high cost. SLD is widely used in commercial OCT devices as the light source because of its relatively low cost compared with Ti:sapphire lasers and operation in different wavelength regions. In this demonstration, we obtained  $\sim 2 \mu\text{m}$  axial resolution using the SLD with 188 nm bandwidth. The similar resolution was achieved using a Ti:sapphire laser with about 150 nm bandwidth.<sup>27</sup>

The ultrahigh resolution OCT designed in our experiment achieves an axial resolution of  $\sim 2 \mu\text{m}$  in tissue, which is finer than that provided by current commercial OCT products, such as Cirrus HD-OCT (Carl Zeiss, Meditec, Dublin, California), the high-resolution SD-OCT for retina and cornea. These commercial SD-OCT devices commonly use a broadband SLD as light source with an axial resolution of  $\sim 5 \mu\text{m}$  in tissue, which may be sufficient for routine clinical applications. With higher axial resolution, it may be suitable for imaging the details of intraretinal layers and the tear film as well as corneal sublayers. As demonstrated in this project, the tear film underneath the contact lens can be clearly visualized, and the approach may allow the doctor to track tear film exchange during contact lens wear. The factor of tear exchange has been a key consideration in contact lens fitting and lens design. There was previously no good method for tracking the two-way mixing of the tear film underneath the lens. The development of such a method is one of the reasons we designed a higher-resolution OCT prototype. In the posterior segment, OCT has been used as a window for some diseases of the central nervous system, such as MS. OCT has been widely used to image the retinal nerve fiber layer (RNFL)

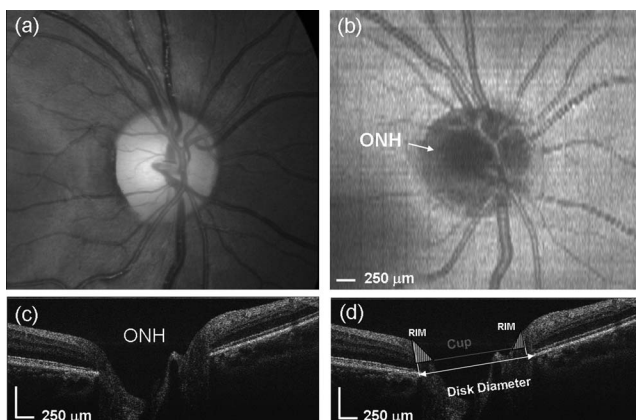


**Fig. 8** ONH acquired by fundus photography and SD-OCT. The ONH in the fundus photo (a), matched the *en face* view obtained with OCT (b). The cup and disk can be seen in the horizontal cross-sectional OCT image (c) and the same image was marked to show the cup/disk ratio (d), which is 0.73. The rim of the ONH was also marked in the image.

layer as a possible biomarker of MS; the measurements have also been used for follow-up. However, recent evidence has indicated that changes of only a few micrometers (2 to 3  $\mu\text{m}$ ) may be observed annually for some types of MS. Such changes may not be detected by commercially available OCT devices.<sup>14</sup> Our system may be validated for use in this type of disease by using a large sample size in the future.

When OCT is applied in human eye imaging, the acquisition time should be short enough to avoid the effect of eye motion in the subject. The highest data transfer rate possible for our OCT system with a CCD is 24,000 A-scan per second (corresponding to a light exposure time of 36  $\mu\text{s}$ ). However, the detection sensitivity may be relatively low in the case of short acquisition times. Taking into account the detection sensitivity, the light exposure time of the CCD should be set to 72  $\mu\text{s}$ . This indicates an acquisition time for a single picture of 0.17 s, which is short enough to acquire a clear image of the human eye without blur. Further improvement may include the incorporation of CMOS in our system to increase the scan speed. The highest data transfer rate achieved was 140 kHz, as reported in the literature.<sup>33</sup>

## 5 Conclusion

This paper describes the use of an ultrahigh resolution SD-OCT using a broadband SLD light source. This OCT system achieves high resolution compared with the Ti:sapphire laser-based OCT system. The experiment axial resolution of our OCT system is 3.1  $\mu\text{m}$  in air and 2.2  $\mu\text{m}$  in tissue, and the axial scan depth is 1.4 mm, as determined by calculating the spectral resolution of the spectrometer. We measured the PSF of a mirror placed at different axial positions at the sample arm and thus obtained the SNR and sensitivity of the OCT system. The sensitivity was 93 dB at the optical path difference of 0.2 mm; a decrease of about 23 dB is found as the scan position is moved farther away from the zero delay plane. Using this ultrahigh resolution SD-OCT system, we imaged the anterior segment and posterior segment of the human eye. The results show that the cornea can be imaged with high quality: even Bowman's membrane and the post-lens tear film can be visualized. During retinal imaging, structural layers, such as the RNFL, photoreceptor layer, and retinal pigment epithelium can clearly be distinguished.

## Acknowledgments

This study has been supported by research grants, including NIH 1R21EY021012 (JW) UM SAC Award (JW), the NIH Center Grant P30 EY014801, and funding provided by Research to Prevent Blindness at the University of Miami. Visiting scholar activity was supported by research grants from the Zhejiang Science and Technology Program, Zhejiang, China (2010C03002) and the Affiliated Eye Hospital of Wenzhou Medical College (YNCX201005).

The authors have no proprietary interest in any materials or methods described within this article.

## References

1. J. G. Fujimoto, "Optical coherence tomography for ultrahigh resolution in vivo imaging," *Nat. Biotechnol.* **21**, 1361–1367 (2003).

2. D. Huang, E. A. Swanson, C. P. Lin, J. S. Schuman, W. G. Stinson, W. Chang, M. R. Hee, T. Flotte, K. Gregory, and C. A. Puliafito, "Optical coherence tomography," *Science* **254**, 1178–1181 (1991).
3. M. A. Shousha, C. L. Karp, V. L. Perez, R. Hoffmann, R. Ventura, V. Chang, S. R. Dubovy, and J. Wang, "Diagnosis and management of conjunctival and corneal intraepithelial neoplasia using ultra high-resolution optical coherence tomography," *Ophthalmology* **118**, 1531–1537 (2011).
4. M. Choma, M. Sarunic, C. Yang, and J. Izatt, "Sensitivity advantage of swept source and Fourier domain optical coherence tomography," *Opt. Express* **11**, 2183–2189 (2003).
5. R. Leitgeb, C. Hitzenberger, and A. Fercher, "Performance of Fourier domain vs. time domain optical coherence tomography," *Opt. Express* **11**, 889–894 (2003).
6. J. F. de Boer, B. Cense, B. H. Park, M. C. Pierce, G. J. Tearney, and B. E. Bouma, "Improved signal-to-noise ratio in spectral-domain compared with time-domain optical coherence tomography," *Opt. Lett.* **28**, 2067–2069 (2003).
7. M. Wojtkowski, T. Bajraszewski, P. Targowski, and A. Kowalczyk, "Real-time *in vivo* imaging by high-speed spectral optical coherence tomography," *Opt. Lett.* **28**, 1745–1747 (2003).
8. V. Hurmeric, S. H. Yoo, C. L. Karp, A. Galor, L. Vajzovic, J. Wang, S. R. Dubovy, and R. K. Forster, "In vivo morphologic characteristics of Salzmann nodular degeneration with ultra-high-resolution optical coherence tomography," *Am. J. Ophthalmol.* **151**, 248–256 (2011).
9. N. Nassif, B. Cense, B. H. Park, S. H. Yun, T. C. Chen, B. E. Bouma, G. J. Tearney, and J. F. de Boer, "In vivo human retinal imaging by ultrahigh-speed spectral domain optical coherence tomography," *Opt. Lett.* **29**, 480–482 (2004).
10. Q. Chen, J. Wang, M. Shen, L. Cui, C. Cai, M. Li, L. Li, and F. Lu, "Tear menisci and ocular discomfort during daily contact lens wear in symptomatic wearers," *Invest. Ophthalmol. Vis. Sci.* **52**, 2175–2180 (2011).
11. J. Ho, A. J. Witkin, J. Liu, Y. L. Chen, J. G. Fujimoto, J. S. Schuman, and J. S. Duker, "Documentation of intraretinal retinal pigment epithelium migration via high-speed ultrahigh-resolution optical coherence tomography," *Ophthalmology* **118**, 687–693 (2011).
12. X. A. Liu and J. U. Kang, "Compressive SD-OCT: the application of compressed sensing in spectral domain optical coherence tomography," *Opt. Express* **18**, 22010–22019 (2010).
13. H. L. Seck, Y. Zhang, and Y. C. Soh, "Optical coherence tomography by using frequency measurements in wavelength domain," *Opt. Express* **19**, 1324–1334 (2011).
14. A. Petzold, J. F. de Boer, S. Schippling, P. Vermersch, R. Kardon, A. Green, P. A. Calabresi, and C. Polman, "Optical coherence tomography in multiple sclerosis: a systematic review and meta-analysis," *Lancet Neurol.* **9**, 921–932 (2010).
15. N. Serbecic, F. Aboul-Enein, S. C. Beutelspacher, C. Vass, W. Kristoferitsch, H. Lassmann, A. Reitner, and U. Schmidt-Erfurth, "High resolution spectral domain optical coherence tomography (SD-OCT) in multiple sclerosis: The first follow up study over two years," *PLOS One* **6**, 19843 (2011).
16. N. Serbecic, F. Aboul-Enein, S. C. Beutelspacher, M. Graf, K. Kircher, W. Geitzenauer, W. Brannath, P. Lang, W. Kristoferitsch, H. Lassmann, A. Reitner, and U. Schmidt-Erfurth, "Heterogeneous pattern of retinal nerve fiber layer in multiple sclerosis. High resolution optical coherence tomography: Potential and limitations," *PLOS One* **5**, 13877 (2010).
17. J. Wang, S. Jiao, M. Ruggeri, M. A. Shousha, and Q. Chen, "In situ visualization of tears on contact lens using ultra high resolution optical coherence tomography," *Eye Contact Lens* **35**, 44–49 (2009).
18. A. Tao, J. Wang, Q. Shen, F. Lu, S. R. Dubovy, and M. A. Shousha, "Topographic thickness of Bowman's layer determined by ultra-high resolution spectral domain optical coherence tomography," *Invest. Ophthalmol. Vis. Sci.* **52**, 3901–3907 (2011).
19. M. X. Shen, L. L. Cui, C. Riley, M. R. Wang, and J. H. Wang, "Characterization of soft contact lens edge fitting using ultra-high resolution and ultra-long scan depth optical coherence tomography," *Invest. Ophthalmol. Vis. Sci.* **52**, 4091–4097 (2011).
20. L. M. Vajzovic, C. L. Karp, P. Haft, M. bou Shousha, S. R. Dubovy, V. Hurmeric, S. H. Yoo, and J. H. Wang, "Ultra high-resolution anterior segment optical coherence tomography in the evaluation of

- anterior corneal dystrophies and degenerations," *Ophthalmology* **118**, 1291–1296 (2011).
21. N. Hutchings, T. L. Simpson, C. Hyun, A. A. Moayed, S. Hariri, L. Sorbara, and K. Bizheva, "Swelling of the human cornea revealed by high-speed, ultrahigh-resolution optical coherence tomography," *Invest. Ophthalmol. Vis. Sci.* **51**, 4579–4584 (2010).
  22. M. Wojtkowski, V. Srinivasan, T. Ko, J. Fujimoto, A. Kowalczyk, and J. Duker, "Ultrahigh-resolution, high-speed, Fourier domain optical coherence tomography and methods for dispersion compensation," *Opt. Express* **12**, 2404–2422 (2004).
  23. J. Ai and L. V. Wang, "Spectral-domain optical coherence tomography: Removal of autocorrelation using an optical switch," *Appl. Phys. Lett.* **88**, 111115 (2006).
  24. W. Drexler, "Ultrahigh-resolution optical coherence tomography," *J. Biomed. Opt.* **9**, 47–74 (2004).
  25. R. Leitgeb, W. Drexler, A. Unterhuber, B. Hermann, T. Bajraszewski, T. Le, A. Stingl, and A. Fercher, "Ultrahigh resolution Fourier domain optical coherence tomography," *Opt. Express* **12**, 2156–2165 (2004).
  26. A. Ozcan, A. Bilenca, A. E. Desjardins, B. E. Bouma, and G. J. Tearney, "Speckle reduction in optical coherence tomography images using digital filtering," *J. Opt. Soc. Am. A* **24**, 1901–1910 (2007).
  27. M. Wojtkowski, V. Srinivasan, J. G. Fujimoto, T. Ko, J. S. Schuman, A. Kowalczyk, and J. S. Duker, "Three-dimensional retinal imaging with high-speed ultrahigh-resolution optical coherence tomography," *Ophthalmology* **112**, 1734–1746 (2005).
  28. N. Nishizawa, S. Ishida, T. Ohta, K. Itoh, M. Kitatsuji, H. Hasegawa, M. Matsushima, and T. Kawabe, "Ex-vivo ultra-high-resolution optical coherence tomography imaging of fine lung structure by use of a high-power Gaussian-like supercontinuum at 0.8- $\mu\text{m}$  wavelength," *Proc. SPIE* **7893**, 78930Y (2011).
  29. B. Bouma, G. J. Tearney, S. A. Boppart, M. R. Hee, M. E. Brezinski, and J. G. Fujimoto, "High-resolution optical coherence tomographic imaging using a mode-locked Ti:Al(2)O(3) laser source," *Opt. Lett.* **20**, 1486–1488 (1995).
  30. W. Drexler, U. Morgner, F. X. Kartner, C. Pitris, S. A. Boppart, X. D. Li, E. P. Ippen, and J. G. Fujimoto, "In vivo ultrahigh-resolution optical coherence tomography," *Opt. Lett.* **24**, 1221–1223 (1999).
  31. A. Kowalevicz, T. Ko, I. Hartl, J. Fujimoto, M. Pollnau, and R. Salathe, "Ultrahigh resolution optical coherence tomography using a superluminescent light source," *Opt. Express* **10**, 349–353 (2002).
  32. Y. Wang, Y. Zhao, J. S. Nelson, Z. Chen, and R. S. Windeler, "Ultrahigh-resolution optical coherence tomography by broadband continuum generation from a photonic crystal fiber," *Opt. Lett.* **28**, 182–184 (2003).
  33. I. Grulkowski, M. Gora, M. Szkulmowski, I. Gorczynska, D. Szlag, S. Marcos, A. Kowalczyk, and M. Wojtkowski, "Anterior segment imaging with spectral OCT system using a high-speed CMOS camera," *Opt. Express* **17**, 4842–4858 (2009).